Climate sensitivity controls global precipitation hysteresis in a changing CO2 pathway

npj | climate and atmospheric science

www.nature.com/npjclimatsci

ARTICLE OPEN

Check for updates

Climate sensitivity controls global precipitation hysteresis in a changing CO_2 pathway

Se-Yong Song[1,6], Sang-Wook Yeh[1]✉, Richard P. Allan[2], Shang-Ping Xie[3], Soon-Il An[4,5] and Hyo-Seok Park[1]

The responses of the Earth's climate system to positive and negative CO_2 emissions are not identical in magnitude, resulting in hysteresis. In particular, the degree of global precipitation hysteresis varies markedly among Earth system models. Based on analysis of Earth's energy budget, here we show that climate sensitivity controls the degree of global precipitation hysteresis. Using an idealized CO_2 removal scenario, we find that the surface available energy for precipitation continues to increase during the initial negative CO_2 emission period following a positive CO_2 emission period, leading to a hysteresis of global precipitation. This feature is more pronounced in Earth System Models with a high climate sensitivity. Our results indicate that climate sensitivity is a key factor controlling the hysteresis behavior of global precipitation in a changing CO_2 pathway. Therefore, narrowing the uncertainty of climate sensitivity helps improve the projections of the global hydrological cycle.

npj Climate and Atmospheric Science (2023)6:156 ; https://doi.org/10.1038/s41612-023-00484-2

INTRODUCTION

Earth is experiencing rapid warming, primarily due to anthropogenic emissions of greenhouse gases. The anthropogenic warming is altering the global climate and pushing human and natural systems beyond their ability to adapt[1–3]. These changes may lead to abrupt and adverse impacts that carry serious risks for humanity. To reduce the vulnerability to anthropogenic climate change, mitigation and adaptation efforts are needed[4,5]. The removal of CO_2 from the atmosphere is currently being considered to limit or even reverse global warming[6–8]. The climate community proposed the Carbon Dioxide Removal Model Intercomparison Project (CDRMIP) in phase 6 of the Coupled Model Intercomparison Project (CMIP6) to explore the potential effects of carbon dioxide removal (CDR) on Earth's climate system[9].

Previous studies have shown that CDR-induced climate response is modulated by the large thermal inertia of the ocean[10]. This response leads to the hysteresis in which the climate response to a negative CO_2 emission is not the same as the response to an antecedent positive CO_2 emission, and the irreversibility where thresholds are crossed that are difficult or impossible to reverse within a human-perceptible timescale. Such CDR-induced climate response induces a substantially delayed and nonlinear response in surface temperatures[10–12], precipitation[13–16], sea level[17], the Atlantic meridional overturning circulation[18,19], Antarctic ice sheets[20,21] and the intertropical convergence zone (ITCZ)[22] in a changing CO_2 pathway. In particular, the precipitation response to a changing CO_2 pathway has been widely investigated due to its importance in climate adaptation and mitigation but important questions remain unanswered: what are physical processes, and how they control the hysteresis of precipitation response.

Transient global precipitation responses to increasing CO_2 forcing are constrained to be 2–3% K^{-1} in CMIP6 climate models[23,24]. This constraint is based on the notion that the precipitation response and its changes are balanced by the energy fluxes between the surface, atmosphere, and the top-of-atmosphere (TOA) on timescales longer than that of radiative-convective equilibrium. Using an idealized CDR scenario, furthermore, the hysteresis behavior in the global precipitation has been found in some studies, with a temporary increase in global mean precipitation following a decrease in atmospheric CO_2 concentrations[13,15]. Such a delayed response can be attributed to a build-up of ocean heat[15], a rapid atmospheric adjustment, and vegetation response to CO_2 radiative forcing[13]. However, little is known about the key factors controlling the degree of hysteresis of CDR-induced precipitation in Earth System Models (ESMs). In this study, we analyzed multiple ESMs from CMIP6 CDRMIP along with a set of climate model experiment to reveal the controlling factor on the degree of global precipitation hysteresis. Here, we propose a new perspective on the degree of hysteresis behavior in the global precipitation, which is determined by the climate sensitivity in ESMs.

RESULTS

Climate sensitivity and hysteresis of surface temperature in a changing CO_2 pathway

Climate sensitivity is a measure of how much warming can be expected in response to a radiative forcing. By definition, an equilibrium climate sensitivity (ECS) is the equilibrium global mean surface air temperature response (ΔT) to radiative forcing induced by a doubling of atmospheric CO_2 concentrations[25,26]. Hereafter, Δ indicates the change relative to the pre-industrial simulations in each ESM, and the list of the symbols and acronyms used in this study is provided in Supplementary Table 1.

Eight ESMs in CMIP6 CDRMIP (Supplementary Table 2) can be divided into two groups based on their representation of the ECS: four ESMs (CanESM5, UKESM1-0-LL, CESM2, and CNRM-ESM2-1) that simulate a higher ECS (High_ECS, hereafter); and four ESMs

[1]Department of Marine Sciences and Convergence Engineering, Hanyang University, Ansan, South Korea. [2]Department of Meteorology and National Centre for Earth Observation, University of Reading, Reading, UK. [3]Scripps Institution of Oceanography, University of California San Diego, La Jolla, CA, USA. [4]Department of Atmospheric Sciences/Irreversible Climate Change Research Center, Yonsei University, Seoul, South Korea. [5]Division of Environmental Science and Engineering, Pohang University of Science and Technology, Pohang, South Korea. [6]Present address: Earth Research Institute, University of California, Santa Barbara, Santa Barbara, CA, USA. ✉email: swyeh@hanyang.ac.kr

(ACCESS-ESM1-5, MIROC-ES2L, GFDL-ESM4, and NorESM2-LM) that simulate a lower ECS (Low_ECS, hereafter) compared with the multi-model mean value (Table 1, and see "Methods"). Indeed, the High_ECS tend to simulate a small negative net climate feedback parameter (λ) compared with the Low_ECS with a large negative λ (Supplementary Fig. 1a–d). Note that a large negative value of λ implies a strong negative or restoring feedback and a small magnitude value of λ indicates a weak net negative feedback. Therefore, the High_ECS is characterized by climate feedback processes in which either climate system radiates thermal energy into space less efficiently and/or it reflects sunlight to space less effectively in response to an imposed radiative forcing. Larger warming is therefore required to restore the energy imbalance at the TOA (ΔN, hereafter) induced by atmospheric CO_2 forcing in the High_ECS, and vice versa in the Low_ECS (Supplementary Fig. 1).

Table 1. Estimates of λ (in W m^{-2} K^{-1}), ERF (in W m^{-2}), and ECS (in K) for CMIP6 models.

	λ	ERF	ECS
CanESM5	−0.64	3.62	5.63
UKESM1-0-LL	−0.68	3.63	5.34
CESM2	−0.62	3.23	5.18
CNRM-ESM2-1	−0.63	2.99	4.76
ACCESS-ESM1-5	−0.73	2.84	3.87
MIROC-ES2L	−1.51	4.05	2.68
GFDL-ESM4	−1.50	3.92	2.62
NorESM2-LM	−1.38	3.50	2.54
Multi-model average	−0.96	3.47	4.08

We delineated the evolution of ΔT to a changing CO_2 pathway in the High_ECS and Low_ECS, respectively. Note that the ΔT time series in Fig. 1a shows the 21-year running mean value. While the evolution of ΔT largely follows CO_2 changes, the associated warming and/or cooling rates are diverse (Fig. 1a). During the positive CO_2 emission period, the High_ECS exhibits a greater warming rate than that of the Low_ECS, as expected. The ΔT increases by 5.9 K for High_ECS and 3.9 K for Low_ECS when CO_2 reaches four times the initial level (value at the year of 140) and then decreases to 1.5 K for High_ECS and 0.6 K for Low_ECS when CO_2 concentration returns to the pre-industrial level (value at the year of 279). The ΔT recovered approximately 85.2% in a changing CO_2 pathway in the Low_ECS but recovers less in the High_ECS, 73.8%. Therefore, the hysteresis of the High_ECS is greater than that of the Low_ECS (Fig. 1b). Here we measure the degree of hysteresis with the area surrounded by the variable trajectory in a changing CO_2 pathway[10] (see "Methods"). Indeed, the High_ECS, with a relatively weak negative net climate feedback parameter, shows a weak climate feedback response compared with the Low_ECS (Supplementary Fig. 2). This should be related to the notion that ESMs with a weak λ have a less-efficient climate-restoring feedback in counteracting the radiative forcing perturbations, leading to much longer response to equilibrate than ESMs with a strong λ[27]. That is, the High_ECS tends to exhibit a strong asymmetric ΔT from the positive to the negative CO_2 emission

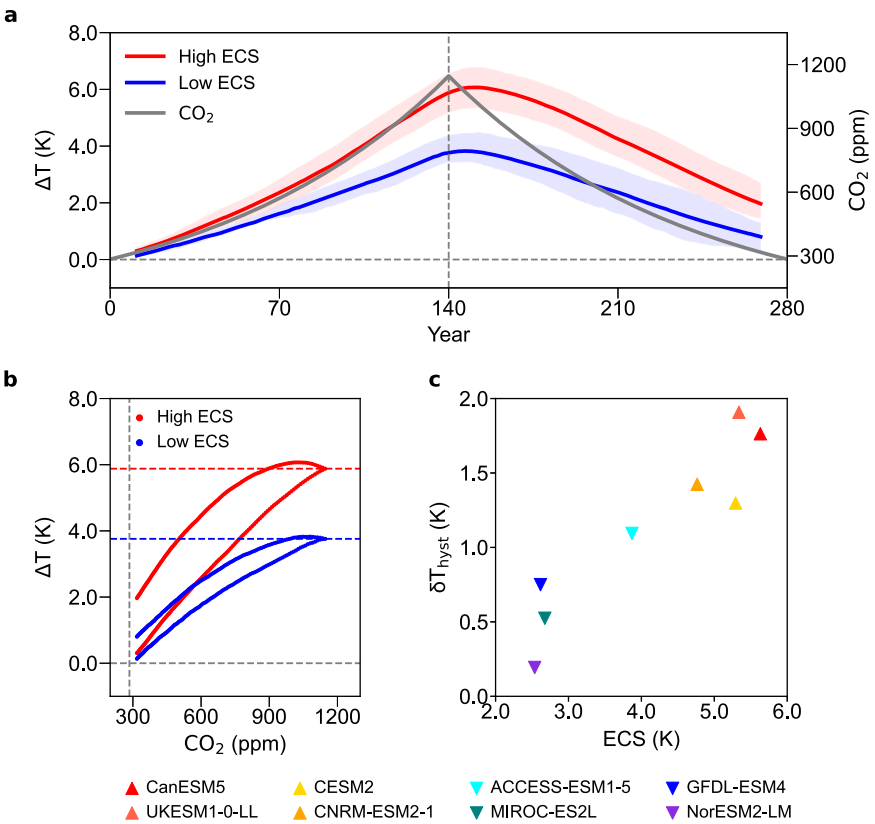

Fig. 1 Temporal evolution and hysteresis behavior of the surface temperature from CMIP6 CDRMIP models. a Time series of ΔT to CO_2 forcing for the High_ECS group (red) and the Low_ECS group (blue). The gray line in **a** denotes the time series of CO_2 concentration. Solid lines and shadings represent the average value and their ensemble spread from each ECS group, respectively. **b** A trajectory of the ΔT in the CO_2 phase space for the High_ECS group and the Low_ECS group. The red and blue horizontal dotted lines denote the ΔT at 140 years for the High_ECS and Low_ECS group, respectively. The gray vertical dotted line denotes the CO_2 concentration at 284.7 ppm. **c** Scatter plot of the ECS versus the difference in the ΔT between the positive (1–139 years) and negative (141–279 years) CO_2 emission period (δT_{hyst}). All values are smoothed by the 21-year running mean. The Δ symbol indicates the change relative to the piControl simulation.

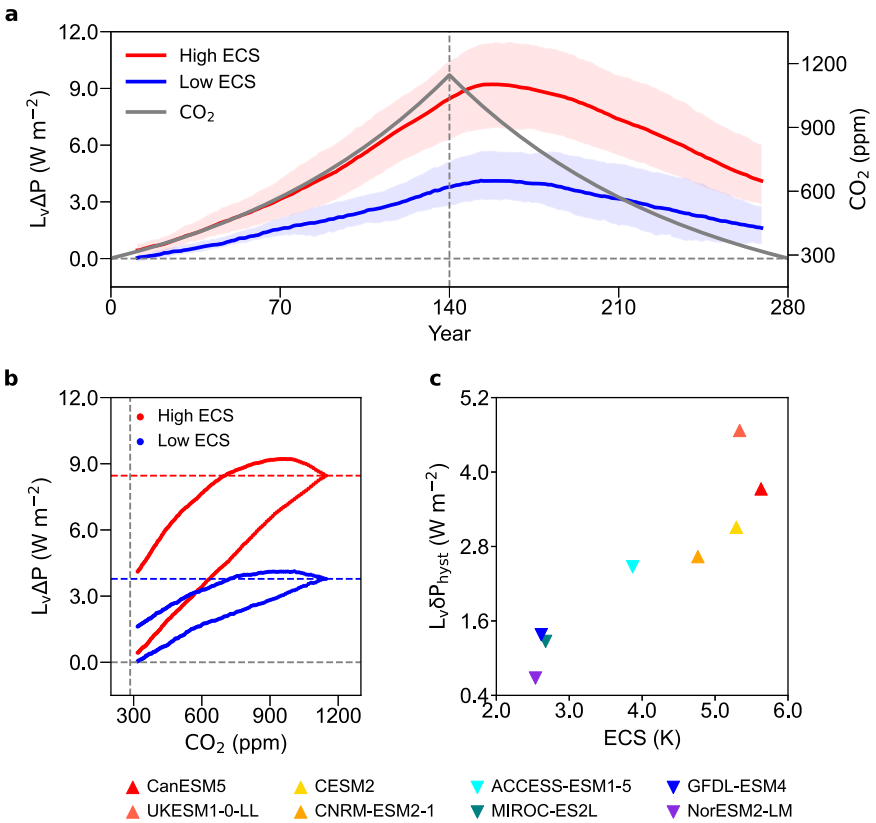

Fig. 2 Temporal evolution and hysteresis behavior of the precipitation from CMIP6 CDRMIP models. a Time series of global annual mean precipitation response multiplied by the latent heat of vaporization ($L_v\Delta P$) to CO_2 forcing for the High_ECS group (red) and the Low_ECS group (blue). The gray line in **a** denotes the time series of CO_2 concentration. Solid lines and shadings represent the average value and their ensemble spread from the High_ECS and Low_ECS group, respectively. **b** A trajectory of the $L_v\Delta P$ in the CO_2 phase space for the High_ECS group and the Low_ECS group. The red and blue horizontal dotted lines denote the precipitation response at 140 years for the High_ECS and Low_ECS group, respectively. The gray vertical dotted line denotes the CO_2 concentration at 284.7 ppm. **c** Scatter plot of the ECS versus the difference in the precipitation response between the positive (1–139 years) and negative (141–279 years) CO_2 emission period (δP_{hyst}). All values are smoothed by the 21-year running mean. The Δ symbol indicates the change relative to the piControl simulation.

period (Fig. 1c) along with a large asymmetry in ΔN (Supplementary Fig. 2) compared to the Low_ECS with a strong λ. This result indicates that the climate feedback responses make a difference in the degree of global warming hysteresis among multiple ESMs. Thus, we argued that the ECS would be a key factor controlling the ΔT hysteresis via modulating climate feedbacks.

There are at least two prominent timescales in the ΔT under the transient scenario in which the atmospheric CO_2 concentration increases at 1% per year. One is the fast response owing to the climate feedback, and the other is the slow response related to the mixing between the upper and deep ocean[28]. Such ΔT change with fast and slow response could also be estimated by the transient climate response (TCR), defined as the ΔT around the time of CO_2 doubling under the transient experiment of 1% increase per year. We found that the TCR could be one of the factors to constrain the degree of hysteresis in CMIP6 CDRMIP ESMs (Supplementary Fig. 3). It is known that there is a nonlinear relationship of TCR and ECS, which is related to the ocean heat uptake efficiency in the TCR[29–32]. Indeed, the difference in the ocean heat uptake efficiency among eight ESMs should be considered when using the TCR to constrain the degree of ΔT hysteresis, which is beyond the scope of this study. Thus, we used the ECS as an indicator to constrain the degree of ΔT hysteresis to emphasize that the difference in the climate feedback response would determine the degree of hysteresis in surface temperature and precipitation in CMIP6 CDRMIP. However, further investigation is needed to clarify the difference in ocean heat uptake efficiency and its non-linearity with the ECS, which influences the degree of hysteresis in surface temperature and precipitation in ESMs.

Hysteresis of the global precipitation constrained by the surface energy budget in a changing CO_2 pathway

The global precipitation response significantly differs in a changing CO_2 pathway between the High_ECS and Low_ECS (Fig. 2a). In High_ECS, the increasing rate in the global precipitation response during the positive CO_2 emission period is 40% larger than its decreasing rate during the negative CO_2 emission period but only 25% larger in Low_ECS (Supplementary Table 3). In addition, the response of the global precipitation after the peak of CO_2 quadrupling remains large in the High_ECS compared with the Low_ECS; consequently, the global precipitation response when CO_2 is restored to its initial states tends to be less recovered in the High_ECS about 54.7% compared with the Low_ECS about 65.7%. Therefore, the High_ECS tends to exhibit greater hysteresis than does the Low_ECS (Fig. 2b). Consistent with the ΔT response, there is a strong dependency of CDR-induced asymmetrical global precipitation response with respect to climate sensitivity due to the magnitude of the ECS (Fig. 2c). The recovery rates of precipitation are lower than those of surface temperature in both High_ECS and Low_ECS, which could be originated from the nonlinear responses of precipitation to surface temperature changes, particularly over the convective regions[33].

We note that ESMs with a large ΔT hysteresis exhibit a greater degree of ΔP hysteresis. This suggests that ΔT hysteresis could be

an important factor in determining the degree of ΔP hysteresis in ESMs. The change in the global precipitation is constrained by the surface energy budget, in which the net surface radiative energy comprising the net surface shortwave and longwave radiation is partitioned into latent and sensible heat fluxes and ocean heat uptake. More than 90% of the extra heat from ΔN is stored in the ocean[34], and ocean heat uptake can be estimated from ΔN (i.e., positive sign denotes heat uptake into the system). Thus, the amount of energy available to drive the global precipitation response (Fig. 2a) is constrained by the surface available energy response (ΔSAE) (Fig. 3a), consisting response of net surface shortwave (ΔSW) and surface longwave (ΔLW) radiative energy, a non-radiative energy of sensible heat (ΔSH), and ΔN. Furthermore, each ΔSAE term shows the distinct asymmetrical response to a changing CO_2 pathway (Fig. 3b–e). Here, the surface radiative fluxes are positive when directed into the surface from the atmosphere, and sensible heat flux is positive when directed away from the surface to the atmosphere.

The ΔSW has been decreased during the CO_2 positive and negative emission period in both High_ECS and Low_ECS (Fig. 3b), respectively, which is mainly due to the increased absorption of shortwave radiation by the increased water vapor in the atmosphere that overwhelms the increased absorption of surface shortwave radiation by the decreased surface albedo and low cloud[35]. The increase in the atmospheric shortwave absorption is larger in the High_ECS than that in the Low_ECS (Supplementary Fig. 4), which is likely due to more abundant atmospheric water vapor content in the High_ECS than the Low_ECS (Supplementary Fig. 5). On the other hand, the surface shortwave cloud radiative effect increases during the both CO_2 positive and negative emission periods in the High_ECS and Low_ECS (Supplementary Fig. 6), leading to the offset of the decrease in the ΔSW due to the increased absorption of shortwave radiation within the atmosphere. We note that this offset is more distinct in the High_ECS, which is mainly due to cloud effect, and it contributes to a smaller decrease in the ΔSW in the High_ECS despite more increased atmospheric shortwave radiation absorption. Furthermore, there is a large diversity of the ΔSW in both High_ECS and Low_ECS compared to other surface energy budget terms (see also Fig. 3f).

The LW response to a changing CO_2 pathway is initially enhanced by the greenhouse effect[36], and it increases surface evaporation and moistens the atmosphere as constrained by the Clausius–Clapeyron relationship. This amplifies initial surface warming through a positive water vapor feedback mechanism[37]. Because water vapor is the most abundant and strongest greenhouse gas in the atmosphere, it exerts the strongest positive feedback and dominates the ΔLW by overwhelming the other LW surface feedbacks, such as the lapse rate and cloud, and thus plays a critical role in the intensification of global precipitation response with an increasing temperature[38]. In particular, the surface LW lapse rate feedback term is nearly negligible compared to the other feedback terms since the surface does not directly respond to radiative changes that occur in the middle to upper troposphere aloft, particularly over the tropics[35]. Meanwhile, the surface longwave cloud radiative effects partially offset the increased ΔLW and weaken the asymmetrical ΔLW (Supplementary Fig. 7). The offsets by the surface longwave cloud radiative effects are more distinct in the High_ECS compared to the Low_ECS (Supplementary Fig. 7). Nevertheless, the High_ECS shows more pronounced asymmetry in ΔLW, which might be originated from the water vapor feedback response. Indeed, the water vapor content of the atmosphere is larger in the High_ECS than in the Low_ECS (Supplementary Fig. 5), a difference that is related to greater enhanced surface warming. Consequently, the ΔLW has been more increased in the High_ECS than the Low_ECS in a changing CO_2 pathway (Fig. 3c). Furthermore, the High_ECS, with a large hysteresis of ΔT, is associated with strong asymmetry in ΔLW (Fig. 3c). The large increase in ΔLW but a small decrease in ΔSW denotes more surplus surface radiative energy response in the High_ECS than the Low_ECS in a changing CO_2 pathway. Subsequently, it is consumed by evaporation by releasing more water vapor into the atmosphere in the High_ECS than the Low_ECS.

The ΔSH is reduced due to decreased air-sea temperature difference in a changing CO_2 pathway[39,40]. The ΔSH is more pronounced in the High_ECS due to larger ΔT increase than that in the Low_ECS (Fig. 3d and see also Fig. 1a). The ΔN has been gradually increased during the positive CO_2 emission period and sharply decreased during the negative CO_2 emission period in both High_ECS and Low_ECS (Fig. 3e). The climate system is taking up heat, mostly into the ocean, until ΔN is negative around the middle of the negative emission period, and ΔN is slightly larger in the High_ECS than that in the Low_ECS. Also, the time when the sign of ΔN changes from positive to negative is earlier in the High_ECS than that in the Low_ECS. This result implies that the climate system in the High_ECS releases energy out of the climate system more quickly than that in the Low_ECS. However, the High_ECS absorbs a larger amount of energy imbalance during the CO_2 positive emission period and it leads to more pronounced asymmetry of ΔN in the High_ECS compared to that of the Low_ECS (Fig. 3f).

The result in Fig. 3b–e indicates that the increase in the net surface radiative energy is largely driven by ΔLW, implying the intensification of the global precipitation response along with a reduced ΔSH, which is partly offset by a reduced ΔSW, and ocean heat uptake when ΔN is positive during the middle of the negative CO_2 emission period[41,42]. In particular, the ΔSAE for the global precipitation response is enhanced more during the negative CO_2 emission period than during the positive CO_2 emission period (Fig. 3f) in both High_ECS and the Low_ECS, leading to the hysteresis of the global precipitation (Fig. 2b). Moreover, the High_ECS shows a large hysteresis of the global precipitation with the more pronounced asymmetrical ΔSAE (Fig. 3f). In detail, the asymmetrical response of the global precipitation is accounted for by the ΔLW, ΔN, and ΔSH ~43.9%, 31.2%, and 18.7%, respectively, in the High_ECS. Therefore, a large ΔP hysteresis in the High_ECS could be related to the asymmetry of ΔLW and ΔN in a changing CO_2 pathway[13,15,16].

Meanwhile, ΔN is expressed by a combination of outgoing longwave radiation response (ΔOLR) and net absorbed shortwave radiation response (ΔASR), which together account for the TOA radiative energy budget. When the outgoing energy is less than the incoming energy at the TOA, the surplus energy in the climate system accumulates in the form of heat. Figure 4 depicts the decomposition of the TOA radiative energy budget into forcing and feedback components (see "Methods"). As for the ΔN, the net downwelling radiation at the TOA is greater in the High_ECS compared to the Low_ECS (Fig. 4a). The forcing component of ΔOLR has been decreased by the greenhouse effect and its evolution is similar between the High_ECS and Low_ECS (Fig. 4b). However, the feedback components of ΔOLR and ΔASR are quite different between the High_ECS and Low_ECS (Fig. 4c, d). Given that the Planck feedback is a function of the surface temperature, the High_ECS emits large ΔOLR to space and exhibits a strong asymmetrical response due to its large ΔT hysteresis (Fig. 4e). Furthermore, the strong water vapor feedback in the High_ECS due to its dependence on ΔT leads to the distinct asymmetrical ΔASR between the positive and negative CO_2 emission period (Fig. 4e).

As a result, the High_ECS shows a relatively weak negative climate-restoring feedback response (Supplementary Fig. 2b) resulting from the large ΔOLR emission but high ΔASR absorption in the climate system during the positive and negative emission periods (Fig. 4c, d). This implies that the High_ECS, which has less-efficient climate-restoring feedback, exhibits a more distinct asymmetrical ΔN at the TOA radiative energy budget (Fig. 4e). In other words, the distinct asymmetrical response in the surface

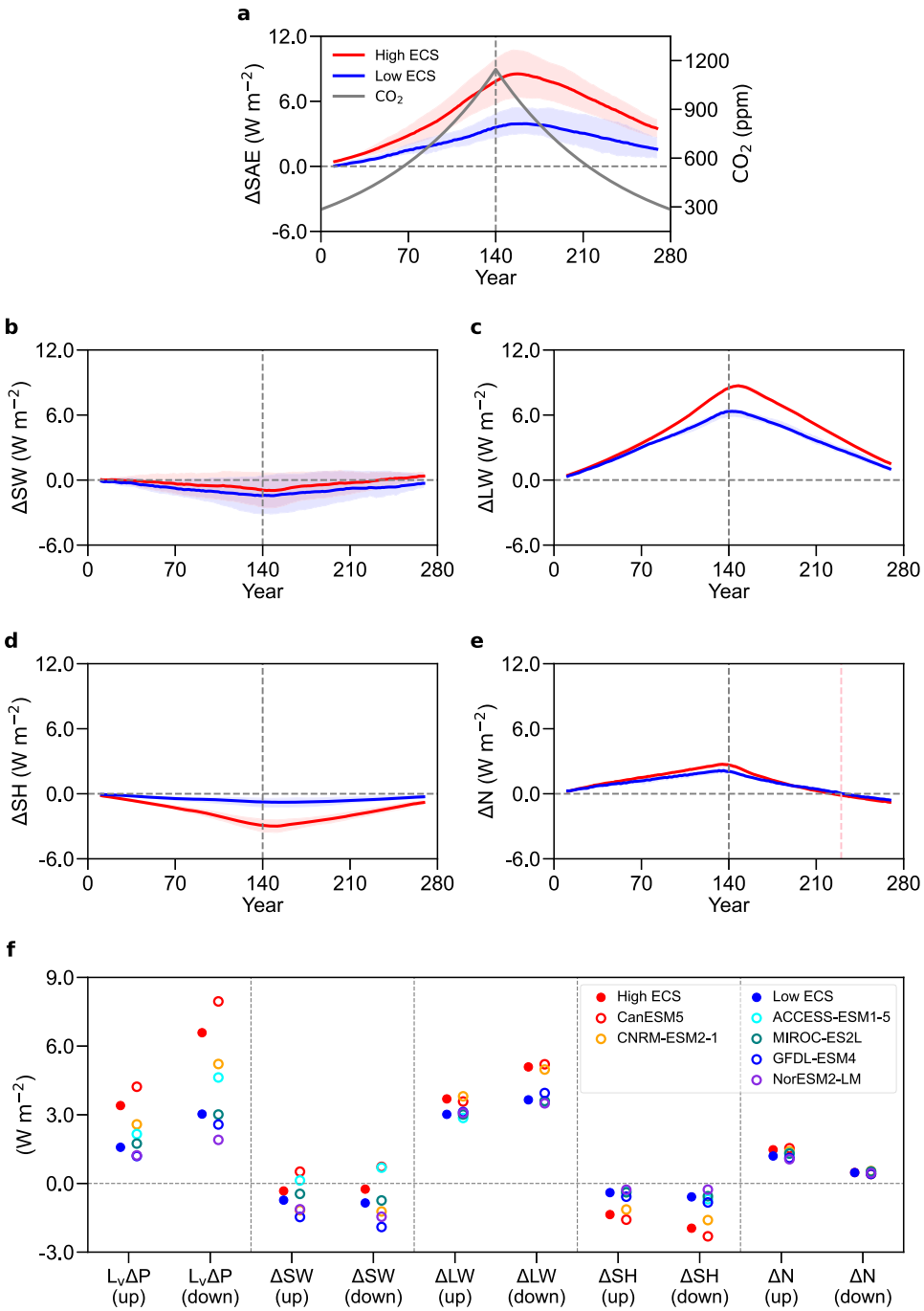

Fig. 3 Temporal evolution and asymmetric response of the surface energy budget from CMIP6 CDRMIP models. a–e Time series of ΔSAE (**a**), ΔSW (**b**), ΔLW (**c**), ΔSH (**d**), and ΔN (**e**) response to CO_2 forcing for the High_ECS group (red) and the Low_ECS group (blue). The ΔSW and ΔLW are positive when directed into from the atmosphere to the surface, and ΔSH is positive when directed away from the surface to the atmosphere. The ΔSAE is calculated as the ΔSW + ΔLW − ΔSH − ΔN, where the positive ΔN denotes the energy in the form of heat is accumulated in the climate system. The gray line in (**a**) denotes the time series of CO_2 concentration. The pink vertical dotted line in (**e**) denotes model year 230. Solid lines and shadings represent the average value and their ensemble spread from each ECS group, respectively. **f** Surface energy budget constraints for the global precipitation under an idealized CO_2 removal scenario. Dots indicate the average value for each surface energy budget term during the positive (1–139 years) and negative (141–279 years) CO_2 emission period. All values are smoothed by the 21-year running mean. The Δ symbol indicates change relative to the piControl simulation. The six models were chosen due to the availability of the surface energy budget of ΔSW and ΔLW.

energy budget, largely driven by the ΔLW and ΔN, leads to more pronounced hysteresis in the global precipitation in the High_ECS than in the Low_ECS (Fig. 2b). This indicates that climate sensitivity determines the degree of asymmetrical ΔLW and ΔN in a changing CO_2 pathway and controls the magnitude of hysteresis behavior in the global precipitation.

Role of forcing and feedback components in a changing CO_2 pathway

We found that the degree of hysteresis behavior in the ΔT and precipitation depends on the representation of climate feedback responses inherent in ECS. However, the precise role of forcing and feedback processes in the surface energy budget remains

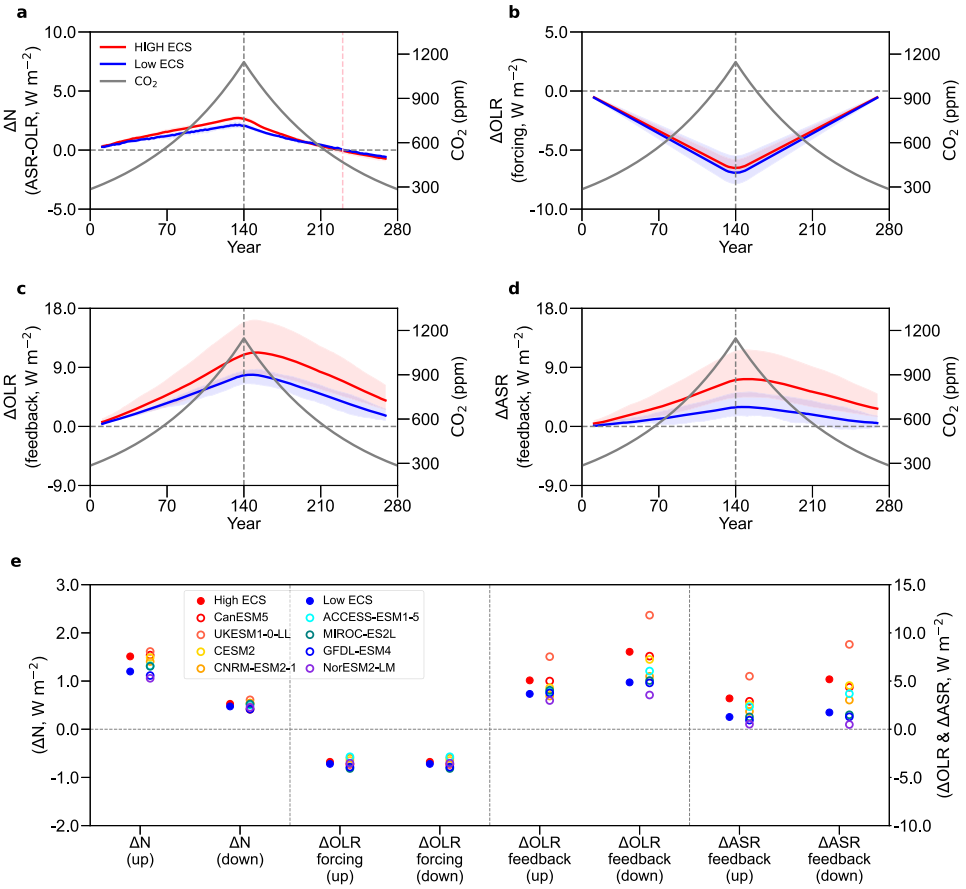

Fig. 4 Temporal evolution and the asymmetric response of the TOA radiative energy budget from CMIP6 CDRMIP models. a–d Time series of ΔN (**a**), the forcing term in ΔOLR (**b**), the feedback term in ΔOLR (**c**), and the feedback term in ΔASR (**d**) response to CO_2 forcing for the High_ECS group (red) and the Low_ECS group (blue). The gray line in (**a**–**d**) denotes the time series of CO_2 concentration. The pink vertical dotted line in (**a**) denotes the model year 230. Solid lines and shadings represent the average value and their ensemble spread from each ECS group, respectively. **e** TOA radiative energy budget under an idealized CO_2 removal scenario. Dots indicate the average value for each TOA radiative energy budget term during the positive (1–139 years) and negative (141–279 years) CO_2 emission period. All values are smoothed by the 21-year running mean. The Δ symbol indicates change relative to the piControl simulation.

elusive. To examine this, we conducted an idealized CDR scenario experiment with a fully coupled global climate model (CGCM) simulation using Community Earth System Model version 1 (CESM1)[43]. In this simulation, transient changes in Earth's energy budget are the result of forcings and feedbacks. We then ran an atmosphere-only global climate model (AGCM) simulation to isolate the forcing components of the Earth's energy budget ("Methods"). This experiment was able to decompose the feedback components derived from the difference between a CGCM (forcing and feedback) and an AGCM (forcing) simulation. This approach has been used as a straightforward way of isolating the forcing components in the Earth's energy budget[44,45].

Figure 5 illustrates the evolution of the surface energy budget obtained from the CESM1 simulations. While the forcing components exhibit a largely symmetrical response, the feedback components show a distinctly asymmetrical response to CO_2 forcing (Fig. 5a and Supplementary Fig. 8). In particular, the asymmetrical response of the global precipitation is driven mostly by the feedback components of ΔLW and ΔN (Fig. 5a). Although the evolution of feedback terms in ΔSW and ΔSH shows the asymmetrical response to CO_2 forcing, these changes are not the dominant driver in the non-reversal response in the global precipitation. Furthermore, it is important to determine what makes the asymmetrical climate feedback response as $\lambda\Delta T$ to a changing CO_2 pathway. This may be the result of either the difference in λ or ΔT between CO_2 positive and negative emission periods. While there is little difference in the climate feedback response responding to ΔT in a changing CO_2 pathway (Supplementary Fig. 9), there are two radiative states for a given CO_2 forcing (Fig. 5b–d). This is because they have different ΔT conditions for the same CO_2 state, so ΔT hysteresis is important in determining the asymmetric climate feedback response in the surface energy budget, which is associated with the hysteresis behavior of global precipitation in ESMs. Therefore, we suggest that climate sensitivity is a key factor for controlling CDR-induced climate response simulated by state-of-the-art global climate models.

DISCUSSION

The differences in representing the climate feedback response determine the degree of climate hysteresis behavior among multiple ESMs. ESMs with a high climate sensitivity, which has less-efficient climate feedback, exhibit less recovery during the negative CO_2 emission period as much as the increases in surface temperature and precipitation during the positive CO_2 emission period. This point is further corroborated by an idealized model experiment, in which the ΔT hysteresis constrains the feedback component in the surface energy budget terms and determines the global precipitation hysteresis. This result implies that ESMs with a high climate sensitivity may take more time to recover to

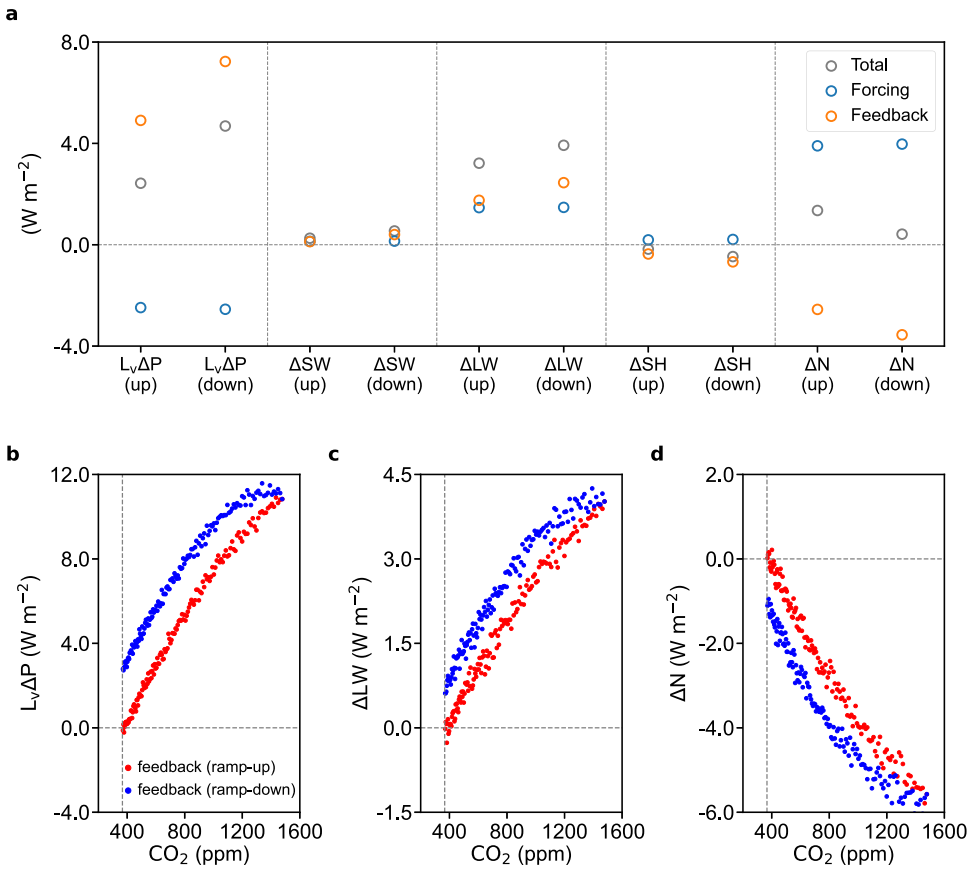

Fig. 5 Hysteresis behavior of the feedback components in the global precipitation and surface energy budget in CESM1 simulation. **a** Surface energy budget constraints for the global precipitation under an idealized CO_2 removal scenario. Dots indicate the total (gray), forcing (light blue) and feedback (orange) components for each surface energy budget term during the positive (1–139 years) and negative (141–279 years) CO_2 emission period. **b**–**d** A trajectory of the feedback terms in the $L_v\Delta P$ (**b**), ΔLW (**c**), and ΔN (**d**) in the CO_2 phase space during the positive (red) and negative (blue) CO_2 emission period. The Δ symbol indicates change relative to CESM1 control simulation.

their original state after the CO_2 concentration recovers to the present climate condition.

This study highlights that CMIP6 ESMs with a high ECS have a greater degree of climate hysteresis in surface temperature and precipitation than those in a low ECS. In this regard, we note that the range of the ECS increases from 2.1–4.7 K in CMIP5 to 1.8–5.6 K in CMIP6 ESMs[46,47]. Particularly, the range in the upper tail of the ECS has significantly been increased from CMIP5 to CMIP6 ESMs, primarily due to a strong positive low cloud feedback in CMIP6 ESMs[47]. This refers to the "hot model" problem in which some CMIP6 ESMs exceed the ECS by more than 4.7 K and there is no such CMIP5 ESMs. Therefore, we cannot exclude the possibility that the climate hysteresis simulated by the CMIP6 ESMs could be influenced by the "hot model" problem.

The regional climate response also may differ between the High_ECS and Low_ECS groups. The hysteresis in the global/regional precipitation can be characterized by the delayed recovery of the ITCZ[22] and distinct asymmetric response in the ocean precipitation[16]. Indeed, the High_ECS shows more distinct asymmetrical responses in the tropical rainfall, particularly over the Pacific Ocean, which is characterized by a southward shift in the ITCZ (Supplementary Fig. 10). The changes in the tropical rainfall pattern are similar to those during an extreme El Niño pattern. This implies that the change in sea surface temperature (SST) patterns is also associated with climate sensitivity (Supplementary Fig. 11), which is termed as pattern effect[48,49], and is in line with asymmetrical tropical rainfall change to CO_2 forcing, which is associated with a delayed slow SST-driven response[50,51]. The group mean SST and precipitation patterns between the High_ECS and the Low_ECS are quite similar. This implies that the regional climate responses in a changing CO_2 pathway between the two groups are closely associated with their amplitude. These further imply that climate sensitivity is a key indicator of hysteresis not only a global scale but also at regional climate scales. An understanding of this climate sensitivity would help develop precise climate mitigation policies for potential climate futures to successfully achieve a post-net-zero emission climate.

METHODS

CMIP6 simulations

In this paper, we utilized four experiments from eight CMIP6 models (ACCESS-ESM1–5, CanESM5, CESM2, CNRM-ESM2-1, GFDL-ESM4, MIROC-ES2L, NorESM2-LM, UKESM1-0-LL and see also Supplementary Table 2)[52]. First, we used the abrupt quadrupling of CO_2 forcing simulation (abrupt 4×CO_2) branched from each model's pre-industrial control simulation (piControl) to estimate the ECS. A detailed methodology for the ECS calculation can be found in the following section. We then used the idealized CDR scenario to examine climate hysteresis under a positive CO_2 (1pctCO_2) and negative (1pctCO_2-cdr) CO_2 emission experiments integrated from the long-term piControl simulation. In these experiments, the atmospheric CO_2 forcing was prescribed to have a 1% increase per year and peak at quadrupling its initial value at 140 years, followed by a 1% decrease per year until the initial CO_2 concentration level (pre-industrial CO_2 level, 284.7 ppm) was reached. The Δ symbol refers to a change relative to a pre-

industrial reference state obtained from the climatological values from the piControl.

Equilibrium climate sensitivity calculation

The ECS is the equilibrium value of ΔT when the radiative equilibrium is reached in response to a doubling of atmospheric CO_2 concentrations relative to pre-industrial levels. This value has been the most commonly applied concept to assess our understanding of the climate system as simulated by global climate models[25,53]. Due to the large heat capacity of the oceans, the climate system takes millennia to achieve equilibrium states in response to an imposed radiative forcing. This makes it difficult to estimate the ECS due to the computational costs of such long-term simulations[26]. For this reason, the ECS is typically estimated from the extrapolation methods using the output from the first 150 years of abrupt 4×CO_2 simulations. This method is based on the forcing and response framework by the following Earth's energy budget equation[54]:

$$\Delta N = \Delta F + \lambda \Delta T \quad (1)$$

where Δ refers to the change relative to a pre-industrial reference state, such that the change in ΔN is partitioned between the effective radiative forcing (ERF, ΔF) and the radiative response (λΔT) related to the climate feedback processes, which are proportional to the change in the ΔT multiplied by the λ.

We use the first 150 years of the abrupt 4×CO_2 simulations, and corrected for model drift by removing the linear trend from the piControl simulation over the period in which it overlapped with the abrupt 4×CO_2 simulation[23,55]. We then calculated the linear regression of ΔN onto ΔT among multiple ESMs (Supplementary Fig. 1). This makes it relatively simple to estimate ERF induced by the atmospheric CO_2 forcing (*y* intercept divided by 2), climate feedback parameter (λ, regression slope), and ECS (*x* intercept divided by 2). Division by 2 is meant to express ERF and ECS with respect to a doubling of atmospheric CO_2 concentrations in line with the standard practice.

Degree of climate hysteresis

A conceptual framework for quantifying hysteresis was suggested in a recent article[10]. In this method, the degree of hysteresis in surface temperature and precipitation can be estimated from the area surrounded by the climate trajectory during the positive and negative CO_2 emission periods. The degree of climate hysteresis among ESMs is determined by the difference in system time lag and nonlinear responses (Figs. 1b and 2b). That is, the relatively long-delayed peak response and less recoverability in the High_ECS group have the larger area surrounded by the climate trajectory in the CO_2 phase space. This result implies that the method in ref. [10] can be applicable for understanding the spread in the CDR-induced climate response among multiple ESMs.

Decomposition of forcing and feedback components at the TOA radiative energy budget

The atmospheric CO_2 forcing directly affects the TOA radiative energy budget by reducing OLR and increases surface warming through the greenhouse effect. The climate system attempts to re-achieve the Earth's energy balance via Planck feedback. In addition, various temperature-mediated feedback processes alter the net TOA radiation through the modulation of the feedback terms in OLR and ASR.

The ΔF could be approximated by its logarithmic dependence on the change in CO_2 concentration[56] as follows:

$$\Delta F = \beta \ln(C/C_0) \quad (2)$$

where *C* and C_0 are the perturbed and control atmospheric CO_2 concentration and β is a constant to be determined. The ΔF includes the shortwave and longwave component of CO_2 radiative forcing. However, the radiative forcing due to the shortwave absorption by CO_2 is only about 4%[56,57]. Thus, we ignored the shortwave fluxes of CO_2 radiative forcing for simplicity. Note that we can obtain consistent results when the ΔF decomposes into its shortwave components calculated as 4% of total CO_2 radiative forcing. The ΔF calculated from the abrupt 4×CO_2 simulation and $C_{4\times CO2}/C_0 = 4$ give β in each global climate model. We can then estimate the transient change in the OLR term to a changing CO_2 pathway. In addition, this enabled us to decompose the feedback term of OLR as the difference between the total (forcing and feedback) change derived from the CMIP6 CDRMIP simulation and the forcing components derived from its logarithmic formula.

Experimental design

To examine the role of forcing and feedback components in the climate hysteresis behavior, we conducted idealized climate model simulations with the CGCM and AGCM experiment using CESM1[43], which configures atmosphere, ocean, sea ice, and land models and prescribes idealized CO_2 forcing. The atmosphere model is version 5 of the Community Atmosphere Model (CAM5), the ocean model is the Parallel Ocean Program version 2, the land model is the Community Land Model version 4, and the sea ice model is the Community Ice Code version 4. The atmosphere and land components have a horizontal resolution of ~1° with 30 vertical levels. The ocean and sea ice components have 60 staggered vertical levels, with a horizontal resolution of 1° of longitude and 0.5° of latitude that decreases to ~0.3° of latitude near the equator.

For the CGCM-type simulations, we conducted present-day control simulations prescribed by the fixed atmospheric CO_2 concentration at the present-day level (367 ppm) over 900 years. We also simulated the idealized CDR transient experiment in which the atmospheric CO_2 forcing increased at a rate of 1% per year until it had quadrupled at 1468 ppm, then decreased back to 367 ppm at the same rate with 28 ensemble members. This experimental setup is similar to the CMIP6 CDRMIP simulation, except for the initial CO_2 concentration level. The 28 ensemble members were conducted with different initial conditions, which were taken arbitrarily from a preset-day control simulation. An ECS value of CESM1 is ~4.0 K[58,59], which lies between the High_ECS and Low_ECS groups. The degree of hysteresis behavior in the ΔT and the global precipitation derived from the CESM1 CGCM simulation is located between the High_ECS and Low_ECS groups (Supplementary Fig. 12). In this fully coupled atmosphere-ocean global climate model simulation, transient changes in the Earth's energy budget are the result of forcing and feedback processes.

A convenient way to diagnose the forcing and feedback components is with an AGCM-type experiment with fixed-SST boundary conditions[44,45]. We therefore performed the additional idealized CDR transient experiment with the AGCM using CAM5 as the atmosphere model for CESM1. For the AGCM-type simulations, we repeated the control, positive and negative CO_2 emission experiments for 100 and 279 years, respectively. We prescribed the ocean and sea ice models with climatological SST and sea ice conditions obtained from a CESM1 CGCM present-day control simulation in the AGCM control, positive and negative CO_2 emission experiments, respectively. This fixed-SST experiment kept the atmosphere and land surface free to respond to perturbations, but large-scale surface temperature-mediated feedbacks were strongly suppressed[60]. The simulated ERF at the TOA closely matched the ERF calculated by the logarithmic dependence on the perturbed CO_2 forcing (Supplementary Fig. 13). We therefore estimated the climate feedback components in the Earth's energy budget as the difference between the total (forcing and feedback) change derived from the CESM1 CGCM simulation and the forcing components derived from the CAM5 AGCM

simulation. This idealized methodology was previously used to decompose the forcing and feedback components in the cloud response under the transient CO_2 reversibility scenario identical to the CMIP6 CDRMIP protocol[44].

DATA AVAILABILITY

The code of CESM1 is available from http://www.cesm.ucar.edu/models. The eight CMIP6 models used in this study are freely available from the Earth System Grid Federation data portal at https://esgf-node.llnl.gov/search/cmip6/.

CODE AVAILABILITY

Python 3.8 was used for plotting. The code used in this study is available from the corresponding author on reasonable request.

Received: 5 May 2023; Accepted: 17 September 2023;
Published online: 30 September 2023

REFERENCES

1. Armstrong McKay, D. I. et al. Exceeding 1.5° C global warming could trigger multiple climate tipping points. *Science* **377**, eabn7950 (2022).
2. Lenton, T. M. et al. Tipping elements in the Earth's climate system. *Proc. Natl. Acad. Sci. USA* **105**, 1786–1793 (2008).
3. Steffen, W. et al. Trajectories of the Earth system in the Anthropocene. *Proc. Natl. Acad. Sci. USA* **115**, 8252–8259 (2018).
4. Lee, J.-Y. et al. Future global climate: scenario-based projections and near-term information. in *Climate Change 2021: The Physical Science Basis. Contribution of Working Group I to the Sixth Assessment Report of the Intergovermental Panel on Climate Change* (eds Masson-Delmotte, V. et al.) 553–672 (Cambridge University Press, 2021).
5. Lenton, T. M. et al. Climate tipping points—too risky to bet against. *Nature* **575**, 592–595 (2019).
6. Rickels, W., Reith, F., Keller, D., Oschlies, A. & Quaas, M. F. Integrated assessment of carbon dioxide removal. *Earth's Future* **6**, 565–582 (2018).
7. Scott, V., Gilfillan, S., Markusson, N., Chalmers, H. & Haszeldine, R. S. Last chance for carbon capture and storage. *Nat. Clim. Change* **3**, 105–111 (2013).
8. Scott, V., Haszeldine, R. S., Tett, S. F. & Oschlies, A. Fossil fuels in a trillion tonne world. *Nat. Clim. Change* **5**, 419–423 (2015).
9. Keller, D. P. et al. The carbon dioxide removal model intercomparison project (CDRMIP): rationale and experimental protocol for CMIP6. *Geosci. Model Dev.* **11**, 1133–1160 (2018).
10. Kim, S.-K. et al. Widespread irreversible changes in surface temperature and precipitation in response to CO_2 forcing. *Nat. Clim. Change* **12**, 834–840 (2022).
11. Tokarska, K. B. & Zickfeld, K. The effectiveness of net negative carbon dioxide emissions in reversing anthropogenic climate change. *Environ. Res. Lett.* **10**, 094013 (2015).
12. Zickfeld, K., MacDougall, A. H. & Matthews, H. D. On the proportionality between global temperature change and cumulative CO_2 emissions during periods of net negative CO_2 emissions. *Environ. Res. Lett.* **11**, 055006 (2016).
13. Cao, L., Bala, G. & Caldeira, K. Why is there a short-term increase in global precipitation in response to diminished CO_2 forcing? *Geophys. Res. Lett.* **38**, L06703 (2011).
14. Song, S.-Y. et al. Asymmetrical response of summer rainfall in East Asia to CO_2 forcing. *Sci. Bull.* **67**, 213–222 (2022).
15. Wu, P., Wood, R., Ridley, J. & Lowe, J. Temporary acceleration of the hydrological cycle in response to a CO_2 rampdown. *Geophys. Res. Lett.* **37**, L12705 (2010).
16. Yeh, S.-W., Song, S.-Y., Allan, R. P., An, S.-I. & Shin, J. Contrasting response of hydrological cycle over land and ocean to a changing CO_2 pathway. *NPJ Clim. Atmos. Sci.* **4**, 1–8 (2021).
17. Boucher, O. et al. Reversibility in an Earth System model in response to CO_2 concentration changes. *Environ. Res. Lett.* **7**, 024013 (2012).
18. An, S. I., Kim, H. J. & Kim, S. K. Rate-dependent hysteresis of the Atlantic meridional overturning circulation system and its asymmetric loop. *Geophys. Res. Lett.* **48**, e2020GL090132 (2021).
19. Rahmstorf, S. et al. Thermohaline circulation hysteresis: a model intercomparison. *Geophys. Res. Lett.* **32**, L23605 (2005).
20. Pollard, D. & DeConto, R. M. Hysteresis in Cenozoic Antarctic ice-sheet variations. *Glob. Planet. Change* **45**, 9–21 (2005).
21. Garbe, J., Albrecht, T., Levermann, A., Donges, J. F. & Winkelmann, R. The hysteresis of the Antarctic ice sheet. *Nature* **585**, 538–544 (2020).
22. Kug, J.-S. et al. Hysteresis of the intertropical convergence zone to CO_2 forcing. *Nat. Clim. Change* **12**, 47–53 (2022).
23. Pendergrass, A. G. The global-mean precipitation response to CO_2-induced warming in CMIP6 models. *Geophys. Res. Lett.* **47**, e2020GL089964 (2020).
24. Samset, B. H. et al. Weak hydrological sensitivity to temperature change over land, independent of climate forcing. *NPJ Clim. Atmos. Sci.* **1**, 1–8 (2018).
25. Knutti, R. & Hegerl, G. C. The equilibrium sensitivity of the Earth's temperature to radiation changes. *Nat. Geosci.* **1**, 735–743 (2008).
26. Rugenstein, M. et al. Equilibrium climate sensitivity estimated by equilibrating climate models. *Geophys. Res. Lett.* **47**, e2019GL083898 (2020).
27. Roe, G. Feedbacks, timescales, and seeing red. *Annu. Rev. Earth. Planet. Sci.* **37**, 93–115 (2009).
28. Manabe, S., Bryan, K. & Spelman, M. J. Transient response of a global ocean-atmosphere model to a doubling of atmospheric carbon dioxide. *J. Phys. Oceanogr.* **20**, 722–749 (1990).
29. Danabasoglu, G. et al. The community earth system model version 2 (CESM2). *J. Adv. Model. Earth Syst.* **12**, e2019MS001916 (2020).
30. Hansen, J. et al. Climate response times: dependence on climate sensitivity and ocean mixing. *Science* **229**, 857–859 (1985).
31. Meehl, G. A. et al. Context for interpreting equilibrium climate sensitivity and transient climate response from the CMIP6 Earth system models. *Sci. Adv.* **6**, eaba1981 (2020).
32. Raper, S. C., Gregory, J. M. & Stouffer, R. J. The role of climate sensitivity and ocean heat uptake on AOGCM transient temperature response. *J. Clim.* **15**, 124–130 (2002).
33. Xie, S.-P. et al. Global warming pattern formation: Sea surface temperature and rainfall. *J. Clim.* **23**, 966–986 (2010).
34. Von Schuckmann, K. et al. Heat stored in the Earth system: where does the energy go? *Earth Syst. Sci. Data* **12**, 2013–2041 (2020).
35. Colman, R. Climate radiative feedbacks and adjustments at the Earth's surface. *J. Geophys. Res. Atmos.* **120**, 3173–3182 (2015).
36. Andrews, T., Forster, P. M. & Gregory, J. M. A surface energy perspective on climate change. *J. Clim.* **22**, 2557–2570 (2009).
37. Held, I. M. & Soden, B. J. Water vapor feedback and global warming. *Annu. Rev. Energy Environ.* **25**, 441–475 (2000).
38. Colman, R. & Soden, B. J. Water vapor and lapse rate feedbacks in the climate system. *Rev. Mod. Phys.* **93**, 045002 (2021).
39. Myhre, G. et al. Sensible heat has significantly affected the global hydrological cycle over the historical period. *Nat. Commun.* **9**, 1–9 (2018).
40. Richter, I. & Xie, S. P. Muted precipitation increase in global warming simulations: a surface evaporation perspective. *J. Geophys. Res. Atmos.* **113**, D24118 (2008).
41. Allen, M. R. & Ingram, W. J. Constraints on future changes in climate and the hydrologic cycle. *Nature* **419**, 228–232 (2002).
42. O'Gorman, P. A., Allan, R. P., Byrne, M. P. & Previdi, M. Energetic constraints on precipitation under climate change. *Surv. Geophys.* **33**, 585–608 (2012).
43. Hurrell, J. W. et al. The community earth system model: a framework for collaborative research. *Bull. Am. Meteorol. Soc.* **94**, 1339–1360 (2013).
44. Andrews, T. & Ringer, M. A. Cloud feedbacks, rapid adjustments, and the forcing–response relationship in a transient CO_2 reversibility scenario. *J. Clim.* **27**, 1799–1818 (2014).
45. Richardson, T., Samset, B., Andrews, T., Myhre, G. & Forster, P. An assessment of precipitation adjustment and feedback computation methods. *J. Geophys. Res. Atmos.* **121**, 11,608–611,619 (2016).
46. Sherwood, S. et al. An assessment of Earth's climate sensitivity using multiple lines of evidence. *Rev. Geophys.* **58**, e2019RG000678 (2020).
47. Zelinka, M. D. et al. Causes of higher climate sensitivity in CMIP6 models. *Geophys. Res. Lett.* **47**, e2019GL085782 (2020).
48. Andrews, T. et al. On the effect of historical SST patterns on radiative feedback. *J. Geophys. Res. Atmos.* **127**, e2022JD036675 (2022).
49. Dong, Y. et al. Biased estimates of equilibrium climate sensitivity and transient climate response derived from historical CMIP6 simulations. *Geophys. Res. Lett.* **48**, e2021GL095778 (2021).
50. Zhou, S., Huang, P., Xie, S.-P., Huang, G. & Wang, L. Varying contributions of fast and slow responses cause asymmetric tropical rainfall change between CO_2 ramp-up and ramp-down. *Sci. Bull.* **67**, 1702–1711 (2022).
51. Chadwick, R., Wu, P., Good, P. & Andrews, T. Asymmetries in tropical rainfall and circulation patterns in idealised CO_2 removal experiments. *Clim. Dyn.* **40**, 295–316 (2013).
52. Eyring, V. et al. Overview of the Coupled Model Intercomparison Project Phase 6 (CMIP6) experimental design and organization. *Geosci. Model Dev.* **9**, 1937–1958 (2016).
53. Grose, M. R., Gregory, J., Colman, R. & Andrews, T. What climate sensitivity index is most useful for projections? *Geophys. Res. Lett.* **45**, 1559–1566 (2018).
54. Gregory, J. et al. A new method for diagnosing radiative forcing and climate sensitivity. *Geophys. Res. Lett.* **31**, L03205 (2004).

55. Andrews, T., Gregory, J. M., Webb, M. J. & Taylor, K. E. Forcing, feedbacks and climate sensitivity in CMIP5 coupled atmosphere-ocean climate models. *Geophys. Res. Lett.* **39**, L09712 (2012).
56. Myhre, G., Highwood, E. J., Shine, K. P. & Stordal, F. New estimates of radiative forcing due to well mixed greenhouse gases. *Geophys. Res. Lett.* **25**, 2715–2718 (1998).
57. Romps, D. M., Seeley, J. T. & Edman, J. P. Why the forcing from carbon dioxide scales as the logarithm of its concentration. *J. Clim.* **35**, 4027–4047 (2022).
58. Gettelman, A. et al. High climate sensitivity in the Community Earth System Model version 2 (CESM2). *Geophys. Res. Lett.* **46**, 8329–8337 (2019).
59. Bacmeister, J. T. et al. CO_2 increase experiments using the CESM: relationship to climate sensitivity and comparison of CESM1 to CESM2. *J. Adv. Model. Earth Syst.* **12**, e2020MS002120 (2020).
60. Andrews, T., Gregory, J. M., Forster, P. M. & Webb, M. J. Cloud adjustment and its role in CO_2 radiative forcing and climate sensitivity: a review. *Surv. Geophys.* **33**, 619–635 (2012).

ACKNOWLEDGEMENTS

This study was supported by National Research Foundation Grant NRF2018R1A5A1024958 and the Korea Environment Industry and Technology Institute (KEITI) through the Climate Change R&D Project for New Climate Regime funded by the Korea Ministry of Environment (MOE) (2022003560001). R.P.A. was funded by the National Centre for Earth Observation Grant NE/RO16518/1 and the RCUK grant NE/T001216/1. We acknowledge the World Climate Research Programme, which, through its Working Group on Coupled Modelling, coordinated and promoted CMIP6. We thank the climate modeling groups for producing and making available their model output, the Earth System Grid Federation (ESGF) for archiving the data and providing access, and the multiple funding agencies who support CMIP6 and ESGF.

AUTHOR CONTRIBUTIONS

S.Y.S. and S.W.Y. contributed equally to designing the research. S.Y.S. performed the data analysis and, together with S.W.Y., interpreted the results. S.Y.S. wrote the manuscript and edited it together with S.W.Y. All the authors discussed the study results and reviewed the manuscript.

COMPETING INTERESTS

The authors declare no competing interests.

ADDITIONAL INFORMATION

Supplementary information The online version contains supplementary material available at https://doi.org/10.1038/s41612-023-00484-2.

Correspondence and requests for materials should be addressed to Sang-Wook Yeh.

Reprints and permission information is available at http://www.nature.com/reprints

Publisher's note Springer Nature remains neutral with regard to jurisdictional claims in published maps and institutional affiliations.